


 Cite this: *Lab Chip*, 2024, 24, 4778

## 3D printing of monolithic gravity-assisted step-emulsification device for scalable production of high viscosity emulsion droplets†

 Yoon-Ho Hwang,<sup>a</sup> Je Hyun Lee,<sup>b</sup> Taewoong Um<sup>c</sup> and Hyomin Lee \*<sup>b</sup>

Microfluidic technology widely used in generating monodisperse emulsion droplets often suffers from complexity, scalability, applicability to practical fluids, as well as operation instability due to its susceptibility to flow perturbations, low clearance, and depletion of surfactants. Herein, we present a monolithic 3D-printed step-emulsification device (3D-PSD) for scalable and robust production of high viscosity emulsion droplets up to 208.16 mPa s, which cannot be fully addressed using conventional step-emulsification devices. By utilizing stereo-lithography (SLA), 24 triangular nozzles with a pair of 3D void flow distributors are integrated within the 3D-PSD to ensure uniform flow distribution followed by monodisperse droplet formation. The outlets positioned vertically downward enables gravity-assisted clearing to prevent droplet accumulation and thereby maintain size monodispersity. Deposition of silica nanoparticles (SiNP) within the device was also shown to alter the surface wettability from hydrophobic to hydrophilic, enabling the production of both water-in-oil (W/O) as well as oil-in-water (O/W) emulsion droplets, operated at a maximum production rate of up to 50 mL h<sup>-1</sup>. The utility of the device is further verified through continuous production of biodegradable polycaprolactone (PCL) microparticles using O/W emulsion as templates. We envision that the 3D-PSD presented in this work marks a significant leap in high-throughput production of high viscosity emulsion droplets as well as the particle analogs.

 Received 5th August 2024,  
 Accepted 22nd September 2024

DOI: 10.1039/d4lc00650j

[rsc.li/loc](https://rsc.li/loc)

### Introduction

Microfluidic technology has been widely used to generate uniform emulsion droplets in various fields of science and engineering that includes food,<sup>1,2</sup> pharmaceuticals,<sup>3,4</sup> biology,<sup>5,6</sup> cosmetics,<sup>7,8</sup> and homecare products<sup>9,10</sup> to name a few. In particular, these monodispersed emulsion droplets produced serve as excellent templates for the synthesis of polymeric particles and microgels due to the exceptional control over the shape, size, and composition, as well as wide selection of compatible droplet solidification methodologies that impart additional functionality.<sup>11–14</sup> Various conventional microfluidic devices based on T-junction,<sup>15,16</sup> co-flow,<sup>17,18</sup> and flow-focusing geometries<sup>17,19,20</sup> have been employed to generate these monodisperse emulsion droplets with coefficient of variation (CV) less than 5%. However, the

productivity is typically low (<10 mL h<sup>-1</sup>) and demands complicated device fabrication and operation procedures.<sup>21–23</sup> These drawbacks have severely impeded the successful translation from lab-scale to commercial manufacturing process.

To resolve the productivity issue, single- or multi-layered devices with a flow-focusing or T-junction geometry have been extensively parallelized in a single platform for throughput enhancement of emulsion droplets.<sup>21–24</sup> Despite these numerous efforts, the major limitation of these emulsification methods based on shear-induced droplet pinch-off mechanism lies in their inherent susceptibility to flow perturbations, thereby compromising the robustness in the operation of these approaches.<sup>25–28</sup> Indeed, small flow rate fluctuations either due to microchannel clogging or nonuniform pressure distribution has been reported to result in highly polydisperse droplets and even irreversible loss of control over the entire emulsification process.

Alternatively, microfluidic step-emulsification devices have emerged for the scalable production of emulsion droplets with exceptional robustness towards perturbations in the fluid flow rate.<sup>25,26,28–30</sup> The unique feature of step-emulsification device lies in its flow-invariant droplet formation mechanism, driven by sudden Laplace pressure drop at the end of the drop generator nozzle.<sup>28–31</sup> This

<sup>a</sup> Department of Polymer Engineering, Pukyong National University, Nam-gu, Busan 48513, Republic of Korea

<sup>b</sup> Department of Chemical Engineering, Pohang University of Science and Technology (POSTECH), Pohang 37673, Republic of Korea.  
 E-mail: [hyomin@postech.ac.kr](mailto:hyomin@postech.ac.kr)

<sup>c</sup> Mechatronics R&D Center, Samsung Electronics, Hwaseong, Gyeonggi-do 18448, South Korea

† Electronic supplementary information (ESI) available. See DOI: <https://doi.org/10.1039/d4lc00650j>

enables the drop generators in a step-emulsification device relatively facile and straightforward to linearly parallelize. In fact, various step geometries including trapezoid, terrace, rectangular, straight-through arrays, edge-based droplet generation (EDGE), and triangular step-emulsification have been implemented in step-emulsification devices based on either poly(dimethylsiloxane) (PDMS) or glass.<sup>25–31</sup> However, the fabrication of these devices typically demands costly and multi-step manufacturing procedures such as photolithography, wet-etching, and thermal bonding in a state-of-the-art cleanroom facility. Moreover, high concentration of the precursors typically used in preparation of microparticles and microgels inevitably involves high viscosity of the dispersed phase which hinders droplet formation during step-emulsification processes. This is further amplified depending on the orientation and position of each individual drop generator with respect to the continuous phase, resulting in uneven flow distribution into each droplet generator as well as build-up of hydrodynamic pressure due to accumulation of pre-formed droplets near to the outlet, as similarly observed by others.<sup>32–34</sup> Thus, there is a compelling need for a new step-emulsification device design and preparation methodology that addresses the inherent limitation of manufacturing complexity while offering facile droplet pinch-off for dispersed phases with high viscosity as well as excellent surface wettability control and efficient clearance mechanism. Efficient clearance mechanism is essential in avoiding droplet accumulation at the outlet as they can potentially impede the formation of subsequent droplets and compromise size uniformity. Along this end, 3D-printing manufacturing technique offers cost-effectiveness, user-friendly operation, rapid and one-step prototyping, and defect-free 3D geometry.<sup>12,24,35</sup> Nevertheless, there still remain limitations and challenges to be resolved in utilizing 3D-printing technique for the design of step-emulsification devices that fulfil all the sophisticated requirements necessary for the robust and scalable production of high viscosity emulsion droplets.

In this work, we report a new 3D-printed step-emulsification device (3D-PSD) for robust and scale-up production of highly viscous emulsion droplets. We fabricate a monolithic 3D-PSD consisting of 24 triangular drop generator nozzles, combined with a pair of 3D flow distributors without complex multi-step fabrication procedures by utilizing a stereo-lithography (SLA) type 3D-printer. The 3D flow distributor is shown to evenly distribute the flow of the dispersed and the continuous phases into each nozzle and step channel, resulting in generation of uniform emulsion droplets. We also demonstrate that the outlets positioned vertically downward enables gravity-assisted clearing to prevent droplet accumulation and thereby maintain size monodispersity even for more dense dispersed phase with high viscosity ( $\mu = 208.16$  mPa s at 20 °C,  $\rho = 1.237$  g cm<sup>-3</sup>). Surface modification of the 3D-PSD hydrophilic using silica nanoparticle (SiNP) coating was shown to also enable facile production of oil-in-water (O/W)

emulsion droplets. The utility of the device was verified through continuous synthesis of biodegradable polycaprolactone (PCL) microparticles using dichloromethane (DCM) as the solvent. We envision that the facile fabrication, cost-effective, and versatile droplet formation from our 3D-PSD provides a new 3D-printing methodology in robust and scale-up production of functional emulsion droplets, particles, and beyond.

## Results and discussion

### Fabrication of a monolithic 3D-printed step-emulsification device (3D-PSD)

One of the key limitations in utilizing conventional step-emulsification devices for robust and scalable production of highly viscous emulsion droplets is the non-uniform droplet pinch-off at the end of the drop generator nozzle and inefficient clearance mechanism that often leads to droplet accumulation and coalescence of the resulting droplets. To realize a monolithic 3D-printed step-emulsification device (3D-PSD) that addresses these issues, we design and fabricate a 3D-printed device with 24 triangular drop generator nozzles, combined with a pair of 3D flow distributors for the dispersed phase and the continuous phase (Fig. 1a). Here, one of the key design principles is to incorporate a 3D flow distributor with a tapered flow guider design optimized in our prior work<sup>12</sup> for even distribution of both the dispersed and the continuous fluids into each nozzle and the step channel. The other important aspect is the perpendicular orientation of each drop maker with respect to the stream of continuous phase that imposes uniform shear to the high viscosity emulsion droplets, offering effective clearing. Without such perpendicular orientation, as typically observed in traditional step-emulsification devices, the droplet formation tends to vary significantly from one nozzle to the other. This is further exemplified by the build-up of hydrodynamic pressure due to accumulation of pre-formed droplets near to the outlet, leading to relatively more polydisperse droplets even for low viscosity fluids (Fig. S1†). On the other hand, as the outlet is positioned vertically downward, gravity also assists in the clearing to prevent droplet accumulation and maintain size monodispersity. During droplet formation, the dispersed phase is emulsified at the end of each horizontally parallelized, triangular-shaped drop generator nozzles (height ( $h$ ): 70  $\mu$ m, width ( $w$ ): 350  $\mu$ m, length ( $l$ ): 175  $\mu$ m, angle ( $\theta$ ): 20°,  $w/h = 5$ )<sup>25,29,31</sup> by the continuous phase that flows through the step channel and into the outlet oriented vertically downward (Fig. 1b and c). To validate this, we first performed computational fluid dynamic (CFD) simulation based on volume-of-fluid (VOF) method using ANSYS FLUENT to verify the capability of the flow distributor in uniformly distributing fluids into each drop generator nozzle and step channel (Fig. 1d). The uniform flow distribution is also experimentally evaluated by

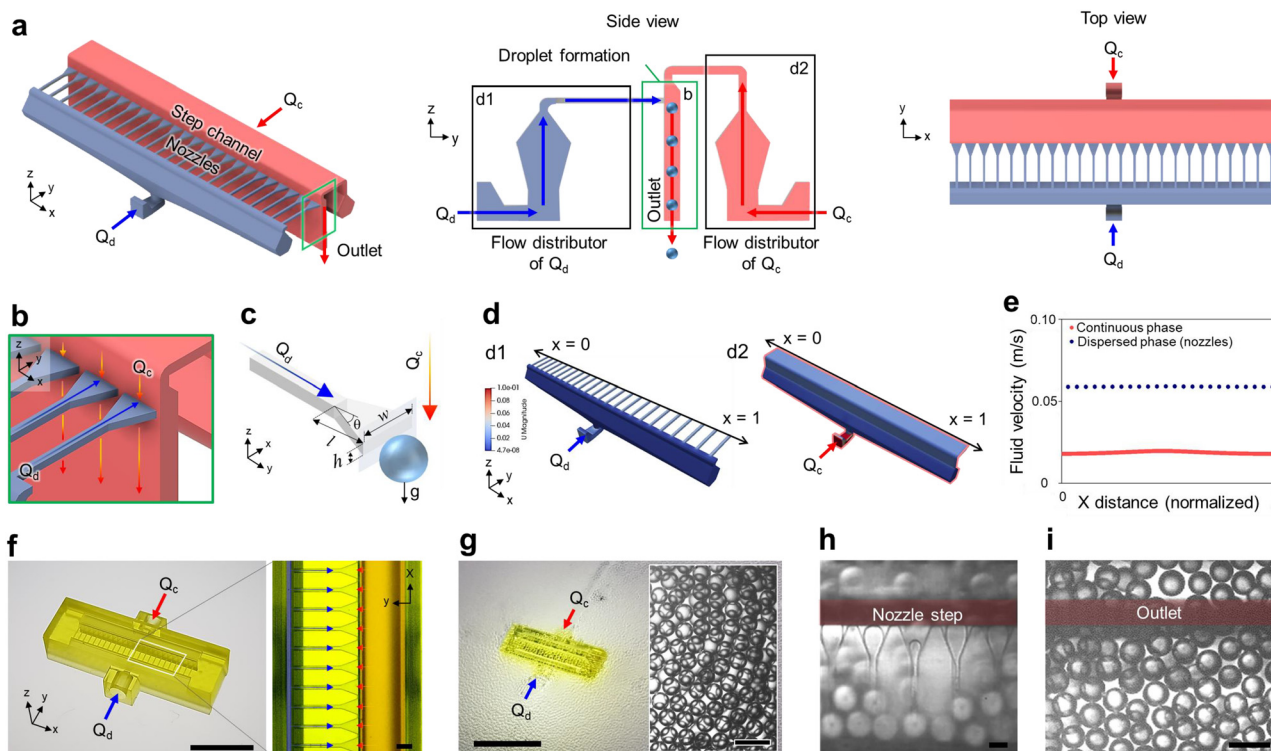


**Fig. 1** (a) Schematics illustrating the 3D-printed step-emulsification device (3D-PSD) at various viewpoints. The device contains 24 drop generator nozzles with a pair of 3D flow distributors. The dispersed phase and the continuous phase are each labelled with blue and red, respectively. (b) Schematics highlighting the dispersed phase flow direction with respect to the continuous phase at the end of the drop generator nozzle. (c) The detailed geometry and the dimensions of each drop generator nozzle. (d) Computer-aided designs (CAD) of the dispersed phase flow distributor (d1) and the continuous phase flow distributor (d2). (e) The computational fluid dynamics (CFD) simulation results of the flow distributors. (f) Photograph of the 3D-PSD (left) and the magnified photograph of the drop generator nozzles. Scale bars represent 5 mm and 350  $\mu\text{m}$ , respectively. (g) Photograph and optical micrograph showing the operation of the device and the W/O emulsions generated from the 3D-PSD, operated at  $Q_d = 50 \text{ mL h}^{-1}$  and  $Q_c = 50 \text{ mL h}^{-1}$ . Scale bars represent 10 mm and 200  $\mu\text{m}$ , respectively. (h and i) Optical micrograph showing (h) the droplet formation at the end of the drop generator nozzle and (i) droplet clearance from the nozzles. Scale bars each represents 200 and 300  $\mu\text{m}$ , respectively.

flowing the dispersed phase ( $Q_d$ ) and continuous phase ( $Q_c$ ) with flow rates set constant at  $Q_d = 25 \text{ mL h}^{-1}$  and  $Q_c = 50 \text{ mL h}^{-1}$ , respectively, to determine the maldistribution factor (MF), defined as:

$$\text{MF} (\%) = \sqrt{\frac{1}{n-1} \sum_{i=1}^n \left( \frac{m_i - \bar{m}}{\bar{m}} \right)^2} \times 100, \quad (1)$$

where  $n$  is the number of outlets,  $m_i$  is the mass flow rate in the  $i$ -th outlet, and  $\bar{m}$  is the average mass flow rate among the outlets. We observe MF (%) value of 0.20 for the 24 nozzles, which fulfils the less than 1% MF value criterion of an even flow distribution, as reported previously (Fig. 1e).<sup>12,36</sup> Then, the newly designed 3D-PSD incorporating the uniform flow distributor is converted into a CAD rendering followed by fabrication using a SLA 3D-printer (MICROARCH® S140) (Fig. 1f). The emulsion production in this newly designed 3D-PSD was evaluated by injecting deionized (DI) water and mineral oil containing 2 wt% Span 80 as the dispersed phase and the continuous phase with flow rates set constant at  $Q_d = 50 \text{ mL h}^{-1}$  and  $Q_c = 50 \text{ mL h}^{-1}$ , respectively, while the opened outlet channel is immersed in a collection container filled with the continuous phase (Fig. 1g). We find that

monodisperse water-in-oil (W/O) emulsion droplets are continuously formed at the end of each nozzle with an average diameter ( $d_{av}$ ) of 190  $\mu\text{m}$ , low CV value of less than 4%, and formation frequency ( $f$ ) of 3.86 kHz (Fig. 1h and i). Overall, these results clearly indicate that a monolithic 3D-PSD which allows even flow distribution into each droplet generator nozzle and step channel can be successfully fabricated using 3D-printing for scalable and robust production of W/O emulsion droplets.

### Robust and scalable production of W/O emulsion droplets with high viscosity

To verify the droplet formation mechanism in our newly designed 3D-PSD, we first monitored the water droplet pinch-off process at the drop generator nozzle using an optical microscope (Fig. 2a). We find that the dispersed phase initially flows into the drop generator nozzle forming a 'tongue-like' bulb. When the dispersed phase reaches the end of the nozzle, it enters the reservoir and grows in size (Fig. 2a, i). During this process, the bulb is still attached to the main thread in the nozzle (Fig. 2a, ii and iii) where the width ( $w$ ) of the bulb neck decreases (Fig. 2a, iv) until the

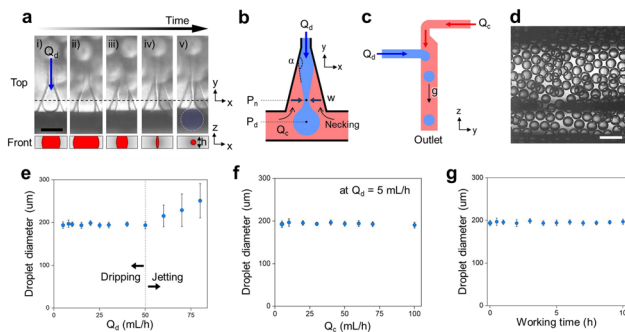


**Fig. 2** (a) Time-lapse optical micrographs of W/O emulsion droplet formation at the drop generator nozzle in 3D-PSD depicting, i) 'tongue-like' bulb formation, ii and iii) bulb growth, iv) thinning of the bulb neck, and v) droplet pinch-off by Rayleigh-Plateau instability. The front panels show the schematic view of the cross-section through the neck. Scale bar represents 300  $\mu\text{m}$ . (b) A schematic illustrating the droplet pinch-off at the drop generator nozzle. (c) Schematic illustration of the droplet formed at the end of the drop maker nozzle draining-out by the continuous phase that flows through the step channel and into the outlet oriented vertically downward. (d) Representative optical micrograph showing the monodisperse W/O emulsion droplets generated from the 3D-PSD, operated at the maximum flow rate of  $Q_{d,\text{max}} = 50 \text{ mL h}^{-1}$  and  $Q_c = 50 \text{ mL h}^{-1}$ . (e) A plot showing the insensitivity of the droplet size distribution on the applied dispersed flow rate below the critical flow rate  $Q_{d,\text{max}} = 50 \text{ mL h}^{-1}$ . The flow transitions from dripping to jetting regime above the  $Q_{d,\text{max}}$ . (f) A plot showing the insensitivity of the droplet size on the continuous phase flow rate from  $5 \text{ mL h}^{-1}$  to  $100 \text{ mL h}^{-1}$  at constant dispersed flow rate of  $Q_d = 5 \text{ mL h}^{-1}$ . (g) A plot showing the operation stability of the 3D-PSD in producing monodisperse W/O emulsion droplets. All error bars represent standard deviation.

thread eventually breaks up (Fig. 2a, iv) due to Rayleigh-Plateau instability that induces pinch-off of the bulb from the dispersed thread (Fig. 2a, v). The detachment of the droplet triggers the formation of a second tongue-like bulb and this cycle is repeated throughout the operation of the device. This process is consistent with the conventional step-emulsification device, where the droplet formation is driven by the difference in Laplace pressure ( $\Delta p = p_n - p_d$ ) in which  $p_n$  and  $p_d$  denotes the pressure of the highly curved interface within the microchannel and the less-curved interface formed when the dispersed phase enlarges into a bulb shape ( $p_d$ ), respectively (Fig. 2b). A flow regime that enables consistent formation of monodisperse droplets through this process is called dripping and when the fluid flow is too fast, the thread does not break-up, leading to a jetting regime and formation of droplets with varying sizes. Also, for robust droplet formation to occur in dripping regime, the nozzle must empty faster than the thread refills which results in coherent decrease in neck width ( $w$ ) followed by break-up. As a result, it is essential to ensure uniform access of continuous phase into each drop generator nozzle and prevent droplet accumulation at the nozzle exits as they can increase the resistance for the flow of the continuous phase into the nozzle, thereby impairing the droplet break-up and increasing the size polydispersity. In our 3D-PSD, however, the continuous phase is identically

supplied into each nozzle through the step channel and the formed emulsion droplets are immediately drained-out by the continuous phase that flows through the step channel and into the outlet oriented vertically downward, granting high production rates while keeping size monodispersity (Fig. 2c).

To also confirm the flow-invariant droplet formation behaviour typically observed in step-emulsification devices,<sup>25–31</sup> we measured the resulting emulsion droplet diameter ( $d$ ) when the flow rate of the dispersed phase ( $Q_d$ ) was varied from 3 to  $80 \text{ mL h}^{-1}$ , while keeping the flow rate of the continuous phase ( $Q_c$ ) constant at  $50 \text{ mL h}^{-1}$ . We observe that below a critical flow rate value of  $Q_{d,\text{max}} = 50 \text{ mL h}^{-1}$ , all nozzles operate in dripping mode (Fig. 2d and S2†). However, when the dispersed flow rate exceeds  $60 \text{ mL h}^{-1}$ , some of the nozzles start to transition into jetting mode, resulting in larger and more polydisperse emulsion droplets with CV of  $>15\%$  (Fig. 2e). Moreover, we observe that the emulsion droplet diameter ( $d$ ) remains unchanged when  $Q_c$  is varied from 5 to  $100 \text{ mL h}^{-1}$  while  $Q_d$  maintained constant at  $5 \text{ mL h}^{-1}$  (Fig. 2f). These findings indicate that the 3D-PSD can consistently produce highly monodisperse droplets ( $d = 190 \mu\text{m}$ , CV  $< 4\%$ , frequency = 3.86 kHz) at a maximum production rate of up to  $50 \text{ mL h}^{-1}$  with exceptional robustness against flow variations, demonstrating its suitability for parallelization.

Another important criterion in robust and scale-up production of emulsion droplets is its long-term operation stability. Indeed, we find no noticeable change in the mean size and the CV value of the droplets generated during 10 h of continuous production compared to the ones formed at the initial stage (Fig. 2g). We note that in some conventional step-emulsification processes, the continuous phase is left stagnant, resulting in surfactant depletion followed by decrease in the stability of the emulsion droplets. However, this issue is not observed in our system, possibly due to the uniform and consistent injection of continuous phase that enables stable formation of emulsion droplets over extended periods.

To further extend to utility of our 3D-PSD in production of polymeric particles and microgels, it is imperative that the device is compatible with dispersed phase fluids that are highly viscous. To verify this potential, we monitored the production rate as well as the size distribution of the resulting W/O emulsion droplets as we progressively increase the viscosity of the dispersed phase through addition of glycerol. For this purpose, we employed 30, 50, 70 and 90 wt% glycerol solutions ( $\mu = 2.56, 6.86, 26.85$  and  $208.16 \text{ mPa s}$  at  $20 \text{ }^\circ\text{C}$ ) as the model dispersed aqueous phases and mineral oil containing 2 wt% Span80 as the continuous phase (Fig. 3a and b). The flow rates of these solutions were varied from 3 to  $50 \text{ mL h}^{-1}$ , while the flow rate of continuous phase ( $Q_c$ ) was set constant at  $50 \text{ mL h}^{-1}$ . We observe that although the droplet size moderately increases with increase in the flow rate of the dispersed phase, the corresponding size distribution remains remarkably narrow (Fig. 3a–c).

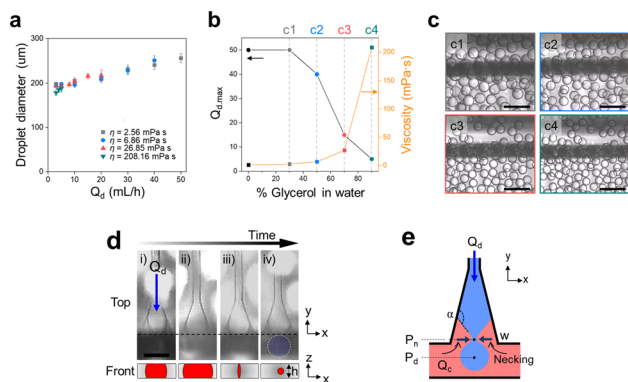


**Fig. 3** (a) A plot showing the size distribution of the W/O emulsion droplets as the viscosity of the aqueous dispersed phase progressively increased through the addition of 30, 50, 70 and 90 wt% glycerol ( $\mu = 2.56, 6.86, 26.85$  and  $208.16$  mPa s at  $20$  °C, respectively). The flow rate of dispersed phase ( $Q_d$ ) was varied in the range of 3 to  $50$  mL  $h^{-1}$ , while the flow rate of continuous phase ( $Q_c$ ) was set constant at  $50$  mL  $h^{-1}$ . (b) A plot showing the maximum operable flow rate ( $Q_{d,max}$ ) and viscosity with variation in the amount of glycerol in the solution. All error bars represent standard deviation. (c) Optical micrographs of W/O emulsion droplets with increasing viscosities of (c1)  $2.56$ , (c2)  $6.86$ , (c3)  $26.85$  and (c4)  $208.16$  mPa s at  $20$  °C, obtained by addition of 30, 50, 70 and 90 wt% glycerol, respectively. (d) Time-lapse optical micrographs showing the high viscosity W/O emulsion droplet formation ( $\mu = 208.16$  mPa s) at the end of the drop generator nozzle in 3D-PSD. i) 'tongue-like' bulb formation, ii) bulb growth, iii) thinning of the bulb neck, and iv) droplet pinch-off by Rayleigh-Plateau instability. The front panels show the schematic view of the cross-section through the neck. Scale bar represents  $300$   $\mu$ m. (e) A schematic illustrating the high viscosity W/O emulsion droplet pinch-off at the drop generator nozzle.

Moreover, the maximum flow rate of dispersed phase ( $Q_{d,max}$ ) determined by the critical point above which the droplet formation mode in each nozzle transitions from dripping to jetting mode is much higher than the previously reported values.<sup>27</sup> While the maximum production rates reported previously for the dispersed phase with viscosities of  $28$  mPa s and  $155$  mPa s were  $0.9$  mL  $h^{-1}$  and  $0.2$  mL  $h^{-1}$ , respectively, our 3D-PSD allowed production of  $50, 40, 15,$  and  $3$  mL  $h^{-1}$  when the viscosity of the dispersed phase were  $2.56, 6.86, 26.85$  and  $208.16$  mPa s, respectively, representing significantly higher throughputs than those achieved previously (Fig. 3b).

To verify the origin of this pronounced throughput value for dispersed phase with high viscosity, we examined the droplet formation behaviour of the most viscous fluid ( $\mu = 208.16$  mPa s at  $20$  °C) tested, analogous to Fig. 2a. Compared to DI water with much less viscosity ( $\mu = 1.00$  mPa s at  $20$  °C), we find that the necking position moves closer towards the end of the nozzle and the neck detaches at much smaller wetting angle ( $\alpha$ ) of  $\sim 120^\circ$  (compared to  $\sim 160^\circ$  for DI water) (Fig. 3d and e). We note that for robust droplet formation in dripping regime, the nozzle must empty faster than the thread refills and the high viscosity of the dispersed phase retards the retraction of the fluid and thus puts significant constraint on the production of monodisperse

emulsion droplets. For our 3D-PSD, the continuous phase uniformly flows through the step channel and into each orthogonally aligned nozzle to facilitate the backflow of the continuous phase into the nozzle, compensating for the slow retraction even in the case of highly viscous fluids to yield uniform droplets. However, we note that maximum operable flow rate of the dispersed phase ( $Q_{d,max}$ ) under dripping regime that leads to monodisperse droplets decreases with increase in viscosity, indicating that further parallelization of the droplet generator nozzles is required to achieve comparable throughput with lower viscosity analog.

### Hydrophilic surface modification of the 3D-PSD for production O/W emulsion-templated microparticles

To fully exploit the potential of 3D-PSD in production of microparticles and microgels, a simple method to alter the surface wetting property of the device hydrophilic needs to be considered as many of the precursor used to prepare microparticles are not only viscous but also insoluble in water. Hydrophilic surface modification of the 3D-PSD enables the continuous phase fluid to favourably wet the inner channel wall of the device, resulting in consistent break-up of the dispersed phase, and ensuring robust production of monodisperse O/W emulsion droplets. Here, we employed silica nanoparticle (SiNP) deposition technique reported previously by us<sup>12</sup> which effectively enhances the hydrophilicity of the 3D-printed substrate. Briefly,  $0.5$  wt% SiNP suspension adjusted to pH  $2.0$  is injected into the 3D-PSD, followed by rinsing with DI water, and then dried in an oven at  $80$  °C for  $15$  minutes. We note that this process results in the formation of SiNP layer that strongly adheres to the 3D-printed substrate (Fig. 4a and b). Indeed, the static water contact angle on an unmodified 3D-printed substrate significantly decreases from  $83 \pm 5$  to  $9 \pm 1^\circ$  after SiNP coating, demonstrating surface hydrophilicity (Fig. 4c and d). The hydrophilic modification of the 3D-PSD ensures the

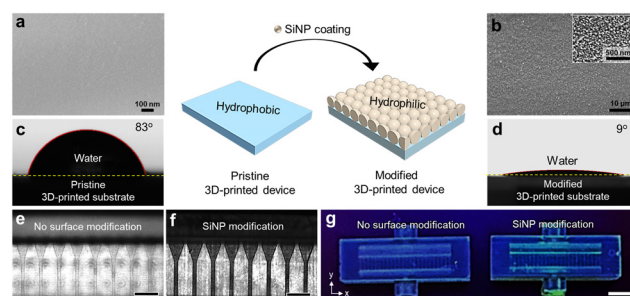


**Fig. 4** Hydrophilic surface modification of the 3D-PSD for production of O/W emulsion droplets. Scanning electron micrographs (SEM) and the static water contact angle analysis on (a and c) pristine 3D-printed substrate and (b and d) modified 3D-printed substrate through deposition of SiNP, respectively. Inset in (b) shows the high-magnification SEM of the modified 3D-printed substrate. (e) Optical micrograph showing the transparency of the unmodified 3D-PSD. (f) Optical micrograph showing the opacity of the modified analog, resulted from the SiNP coating. (g) Photographs of the unmodified 3D-PSD (left) and the modified 3D-PSD (right) under the UV lamp ( $\lambda = 365$  nm).

aqueous phase to completely wet the modified inner surface. We also note that the utilization of acidic SiNP suspension with a pH of 2.0 is crucial for creating a dense SiNP coating layer by minimizing the electrostatic repulsion near the isoelectric point (IEP).<sup>37</sup> The existence of SiNP coating on 3D-PSD can be easily visualized by the opacity of the coated device, in contrast to the transparent uncoated device (Fig. 4e and f). To further confirm the uniform SiNP coating within the 3D-PSD, fluorescein sodium salt (green fluorescent dye) is incorporated into the SiNP suspension for visualization of the SiNP layer. Comparing the modified 3D-PSD with the unmodified analog upon exposing to UV lamp ( $\lambda = 365$  nm) confirms the complete coverage of SiNP onto the wall of 3D-PSD (Fig. 4g). Then, to verify whether the hydrophilic modification of 3D-PSD enables the facile formation of O/W emulsions, we choose DCM solvent containing red fluorescent dye (Nile red) and 2 wt% PVA solution as the model dispersed oil phase and the continuous aqueous phase, respectively (Fig. 5a). Here, DCM was chosen as the dispersed phase as it is a common organic solvent for dissolving a wide range of monomers and polymers in preparation of functional microparticles.<sup>12,22</sup> Owing to the favorable wetting of the continuous fluid to the modified channel, we observe stable pinch-off of the DCM bulb at the end of step nozzle, yielding uniform O/W emulsion droplets (Fig. 5b). Measuring the diameter ( $d$ ) of the resulting droplet as the flow rate of dispersed phase ( $Q_d$ ) was varied from 5 to 60 mL h<sup>-1</sup> (flow rate of continuous phase ( $Q_c$ ) kept constant at 50 mL h<sup>-1</sup>) reveals that monodisperse O/W emulsion droplets ( $d = 190$   $\mu$ m, CV < 4%, frequency = 2.36 kHz) can be produced at a maximum production rate of up to 40 mL h<sup>-1</sup>

in the modified 3D-PSD (Fig. 5c and S3<sup>†</sup>). As the hydrophilic coating remains intact even after continuous flowing of DCM for 10 h and retain surface hydrophilicity,<sup>12</sup> we believe that our 3D-PSD offers new opportunities for scale-up production of O/W emulsion droplets as well as the emulsion-templated functional microparticles. To demonstrate this potential, we utilize the modified 3D-PSD in robust and scalable production of polymeric particles comprising of PCL, which is U.S. Food and Drug Administration (FDA) approved biodegradable material. We operate the device using 4 wt% PCL in DCM solvent as the dispersed phase and 2 wt% PVA solution as the continuous phase each at a flow rate of  $Q_d = 40$  mL h<sup>-1</sup> and  $Q_c = 50$  mL h<sup>-1</sup>, respectively. Collection of these initial DCM droplets containing PCL ( $d = 210$   $\mu$ m, CV = 4%), followed by removal of DCM solvent from the droplets, results in solidified PCL microparticles ( $d = 73$   $\mu$ m, CV = 4%) (Fig. 5d and e). When the DCM solvent is fully removed from the emulsion droplets, the final volume decreases down to nearly 30%. We observe that the diameter of the PCL microparticles ( $d_{\text{exp}}$ ) matches well with the predicted diameter ( $d_p$ ), which is expressed as,  $d_p^3 = d_T^3(\rho_{4\text{wt}\%}/\rho_{\text{PCL}})$ . Here,  $d_T$ ,  $\rho_{\text{PCL}}$ ,  $\rho_{4\text{wt}\%}$  represents the diameter of droplet template, the density of PCL microparticle, and the weight per volume concentration of PCL in DCM droplet, respectively (Fig. 5f).

## Conclusions

In summary, we report a new 3D-printed step-emulsification device (3D-PSD) design that allows robust and scale-up production of emulsion droplets comprising of high viscosity fluids ( $\mu = 208.16$  mPa s). The integration of 24 precisely engineered triangular nozzles with 3D flow distributors were shown to ensure uniform flow distribution into each nozzle and step channel, addressing the critical challenges of throughput and susceptibility to flow perturbations. The gravity-assisted design of the outlets grants operation stability by preventing droplet accumulation near the nozzle exits, thereby enabling the throughput of monodisperse emulsion droplets up to 50 mL h<sup>-1</sup>. In addition, the uniform and consistent injection of continuous phase during droplet formation in 3D-PSD is anticipated to resolve the inherent surfactant depletion issue associated with stagnant continuous phases in conventional step-emulsification devices, thereby offering long-term operation stability. Furthermore, the hydrophilic surface wetting property of our 3D-PSD modified *via* SiNP coating enables reliable production of O/W emulsion droplets and biodegradable PCL microparticles. We note that while we have primarily demonstrated the applicability of our 3D-PSD in producing polymeric microparticles templated from O/W emulsions by taking advantage of the hydrophilic surface modification through SiNP coating, 3D-PSD is also applicable for production of hydrogel microbeads, or microgels, by utilizing W/O emulsions as templates. As many of the hydrogel precursor solutions are highly viscous in nature, we anticipate that our 3D-PSD will

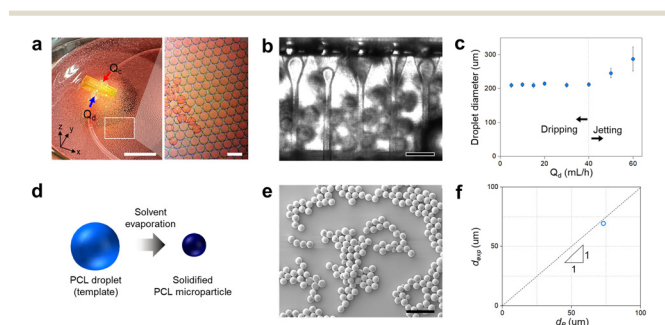


**Fig. 5** (a) Photographs of the O/W emulsion droplets generated from the hydrophilically modified 3D-PSD. Scale bars each represents 10 mm and 300  $\mu$ m, respectively. (b) Optical micrograph showing the O/W emulsion droplet formation at the drop generator nozzle in hydrophilically modified 3D-PSD. Scale bar represents 350  $\mu$ m. (c) A plot showing the insensitivity of the O/W emulsion droplet size distribution on the applied dispersed phase flow rate below a critical flow rate  $Q_{d,\text{max}} = 40$  mL h<sup>-1</sup> while keeping the continuous phase flow rate at  $Q_c = 50$  mL h<sup>-1</sup>. The flow transitions from dripping to jetting regime above the  $Q_{d,\text{max}}$ . The error bars represent standard deviation. (d) A schematic illustrating the preparation of polycaprolactone (PCL) microparticles from O/W emulsion droplet templates *via* solvent evaporation. (e) SEM of the PCL microparticles after evaporation. Scale bar represents 300  $\mu$ m. (f) Plot of the experimentally measured particle diameter ( $d_{\text{exp}}$ ) versus the predicted particle diameter ( $d_p$ ).

allow scalable and robust production of microgels with excellent mechanical properties, biocompatibility, and tunable biofunctionality for various biomedical applications including cell therapy, drug delivery and tissue regeneration to name a few.<sup>38</sup> We also note that while triangular drop generator nozzles with 70  $\mu\text{m}$  height were employed to result in 190  $\mu\text{m}$  sized droplets, we believe that fabrication of the nozzles with a higher resolution 3D printer will allow production of even smaller sized droplets as the resulting droplet size is primarily governed by the geometry of the drop generator nozzle. Overall, we anticipate that the freedom of 3D channel design, cost-effectiveness, simple fabrication, and versatile productivity of 3D-PSD will pave the way in 3D-printing based manufacturing platform for the scalable production of emulsion-templated products in numerous industrial sectors.

## Experimental section

### Materials

Mineral oil ( $\geq 99\%$ ), Span 80 (nonionic surfactant), fluorescein sodium salt (green fluorescent dye), Nile red (red fluorescent dye), glycerol ( $\geq 99.5\%$ ), hexane ( $\geq 95\%$ ), isopropyl alcohol (IPA,  $\geq 99.5\%$ ), polycaprolactone (PCL), dichloromethane (DCM  $\geq 99.8\%$ ), poly(vinyl alcohol) (PVA,  $M_w = 13\,000\text{--}23\,000$ ), and Ludox® colloidal silica (TM-50) were purchased from Sigma-Aldrich. Polyethylene tube (ID = 500  $\mu\text{m}$ , OD = 1/16 inch) was purchased from Saint-Gobain PPL CORP. Deionized (DI) water (EXL®, 18.2  $M\Omega\text{ cm}$  at 28  $^\circ\text{C}$ ) was used for all experiments.

### Fabrication of 3D-printed step-emulsification device (3D-PSD)

By using a computer-aided design (CAD) software (Autodesk Inventor), 3D-printed step-emulsification devices are rendered. The CAD file is printed-out using a stereolithography apparatus (SLA) type 3D-printer (MICROARCH@ S140) with a commercially available acrylate-based polymer resin (HTL yellow). The newly designed device is printed-out in a layer-by-layer manner each layer with thickness of 10–40  $\mu\text{m}$ , where the UV-curable polymer resin is cross-linked by exposure to UV-LED ( $\lambda = 405\text{ nm}$ ). The non-crosslinked resin is rinsed with IPA and dried with compressed air. The tubing is firmly connected with both inlets to infuse the dispersed and continuous phase into the device.

### Production of W/O and O/W emulsion droplets from 3D-PSD

By using syringe pumps (KDS Legato™ 100), the dispersed and continuous phase fluids are supplied and controlled. The resulting W/O and O/W emulsion droplets are collected in containers which is filled with each continuous phase fluid. The formation of emulsion droplets is monitored using an inverted microscope (Eclipse Ts2, Nikon) equipped with a high-speed camera (FASTCAM Mini UX50, Photron). At least 100 emulsions are sampled to determine the mean diameter using ImageJ software. All data are presented as the mean  $\pm$  standard deviations (SD). The error bars represent SD.

### Production of PCL microparticles

To generate the PCL microparticles, 4 wt% PCL and 2 wt% PVA are each dissolved in DCM solvent and DI water for dispersed phase and continuous phase, respectively. By using syringe pumps, the polymeric dispersed phase and aqueous phase are infused into the 3D-PSD. After the collection of emulsion droplets, the residual organic solvent are removed for 20 min using a rotary-evaporator. The PCL microparticles are rinsed three times with DI water, followed by drying under vacuum desiccator for 24 h. The resulting PCL microparticles were imaged using a scanning electron microscope (SEM, JEOL 7500F HRSEM). Similarly, more than 100 samples are analysed using ImageJ software to determine the mean diameter of the microparticles. All data are presented as the mean  $\pm$  standard deviations (SD). The error bars represent SD.

### Computational fluid dynamics (CFD) simulation conditions for acquisition of flow distribution

The 3D unsteady numerical simulation is performed to acquire the flow distribution in each drop generator and 3D flow distributor. All the physical conditions of the fluids and the parameters used for CFD simulations are detailed in Table S1.†

**Governing equations.** The dispersed fluids and the continuous fluids are assumed as incompressible Newtonian fluids. The mass and momentum conservation can be calculated with the sets of Navier–Stokes equation below;

$$\nabla \cdot u = 0 \quad (2)$$

$$\rho \frac{\partial u}{\partial t} + \rho u \cdot \nabla u = -\nabla p + \mu \nabla^2 u + F_\gamma + F_g, \quad (3)$$

where  $\rho$  is the density of fluid,  $\mu$  is the viscosity of fluid,  $F_\gamma$  is the surface tension force and  $F_g$  is the gravitational force. The simulation was performed using a commercial software package in ANSYS FLUENT, Multiphase solver (interFoam).

### Characterization of the SiNP modified 3D-PSD

The static water contact angle of the 3D-printed substrate before and after SiNP modification are obtained by using a contact angle goniometer (SMARTDROP Femtolab). For surface topology analysis, the sample are prepared by breaking the unmodified and modified 3D-PSD followed by analysis using the SEM. The SiNP layer immobilization was also confirmed through fluorescein adsorption using a fluorescence microscope (Eclipse Ts2, Nikon).

## Data availability

The data supporting this article have been included as part of the ESI.†

## Author contributions

Y.-H. Hwang designed, conducted the overall experiments, and performed the data analysis. J. H. Lee helped conducting the experiments. T. Um helped the CFD analysis. H. Lee conceived the project. Y.-H. H., and H. L. wrote the paper, and all authors reviewed the manuscript.

## Conflicts of interest

There are no conflicts to declare.

## Acknowledgements

This work was supported by the National Research Foundation of Korea (NRF) grant funded by the Korea government (MSIT) (No. RS-2023-00208746), (No. RS-2023-00260454). This research was also supported by the Technology Innovation Program (or Industrial Strategic Technology Development Program-Bio-industry technology development program) (20020231, Optimization of structure-based mRNA vaccine production and efficacy evaluation) funded by the Ministry of Trade, Industry & Energy (MOTIE, Korea), and also the industrial grant funded by the LG Chem Ltd.

## Notes and references

- S. He, N. Joseph, S. Feng, M. Jellicoe and C. L. Raston, *Food Funct.*, 2020, **11**, 5726–5737.
- T. A. Comunian, A. Abbaspourrad, C. S. Favaro-Trindade and D. A. Weitz, *Food Chem.*, 2014, **152**, 271–275.
- T. S. Kaminski and P. Garstecki, *Chem. Soc. Rev.*, 2017, **46**, 6210–6226.
- A. Maged, R. Abdelbaset, A. A. Mahmoud and N. A. Elkasabgy, *Drug Delivery*, 2022, **29**, 1549–1570.
- T. Rossow, P. S. Lienemann and D. J. Mooney, *Macromol. Chem. Phys.*, 2017, **218**, 1600380.
- J. E. Mealy, J. J. Chung, H.-H. Jeong, D. Issadore, D. Lee, P. Atluri and J. A. Burdick, *Adv. Mater.*, 2018, **30**, 1705912.
- I. T. Carvalho, B. N. Estevinho and L. Santos, *Int. J. Cosmet. Sci.*, 2016, **38**, 109–119.
- J. H. Lee, Y.-H. Hwang, M. Noh, J. H. Lee, J. B. Lee and H. Lee, *Biomater. Sci.*, 2023, **11**, 7531–7540.
- W. Li, L. Zhang, X. Ge, B. Xu, W. Zhang, L. Qu, C.-H. Choi, J. Xu, A. Zhang, H. Lee and D. A. Weitz, *Chem. Soc. Rev.*, 2018, **47**, 5646–5683.
- L. Shang, Y. Cheng and Y. Zhao, *Chem. Rev.*, 2017, **117**, 7964–8040.
- J. Kwon and H. Lee, *Korean J. Chem. Eng.*, 2023, **40**, 445–451.
- Y.-H. Hwang, T. Um, G.-N. Ahn, D.-P. Kim and H. Lee, *Chem. Eng. J.*, 2022, **431**, 133998.
- X. Mao, M. Wang, S. Jin, J. Rao, R. Deng and J. Zhu, *J. Polym. Sci.*, 2022, **60**, 1653–1669.
- R. K. Shah, H. C. Shum, A. C. Rowat, D. Lee, J. J. Agresti, A. S. Utada, L.-Y. Chu, J.-W. Kim, A. Fernandez-Nieves, C. J. Martinez and D. A. Weitz, *Mater. Today*, 2008, **11**, 18–27.
- P. Garstecki, M. J. Fuerstman, H. A. Stone and G. M. Whitesides, *Lab Chip*, 2006, **6**, 437–446.
- V. van Steijn, C. R. Kleijn and M. T. Kreutzer, *Lab Chip*, 2010, **10**, 2513–2518.
- S. Hettiarachchi, G. Melroy, A. Mudugamuwa, P. Sampath, C. Premachandra, R. Amarasinghe and V. Dau, *Sens. Actuators, A*, 2021, **332**, 113047.
- W. Lee, L. M. Walker and S. L. Anna, *Phys. Fluids*, 2009, **21**, 032103.
- M. Muluneh and D. Issadore, *Lab Chip*, 2013, **13**, 4750–4754.
- A. Lashkaripour, C. Rodriguez, L. Ortiz and D. Densmore, *Lab Chip*, 2019, **19**, 1041–1053.
- D. M. Headen, J. R. García and A. J. García, *Microsyst. Nanoeng.*, 2018, **4**, 17076.
- S. Yadavali, H.-H. Jeong, D. Lee and D. Issadore, *Nat. Commun.*, 2018, **9**, 1222.
- J. Wu, Y.-H. Hwang, S. Yadavali, D. Lee and D. A. Issadore, *Adv. Funct. Mater.*, 2024, **34**, 2309718.
- T. Femmer, A. Jans, R. Eswein, N. Anwar, M. Moeller, M. Wessling and A. J. C. Kuehne, *ACS Appl. Mater. Interfaces*, 2015, **7**, 12635–12638.
- E. Amstad, M. Chemama, M. Eggersdorfer, L. R. Arriaga, M. P. Brenner and D. A. Weitz, *Lab Chip*, 2016, **16**, 4163–4172.
- F. Schuler, F. Schwemmer, M. Trotter, S. Wadle, R. Zengerle, F. von Stetten and N. Paust, *Lab Chip*, 2015, **15**, 2759–2766.
- A. G. Hâti, T. R. Szyborski, M. Steinacher and E. Amstad, *Lab Chip*, 2018, **18**, 648–654.
- J. Wu, S. Yadavali, D. Lee and D. A. Issadore, *Appl. Phys. Rev.*, 2021, **8**, 031304.
- Z. Liu, C. Duan, S. Jiang, C. Zhu, Y. Ma and T. Fu, *J. Ind. Eng. Chem.*, 2020, **92**, 18–40.
- G. T. Vladislavljević, E. E. Ekanem, Z. Zhang, N. Khalid, I. Kobayashi and M. Nakajima, *Chem. Eng. J.*, 2018, **333**, 380–391.
- Z. Shi, X. Lai, C. Sun, X. Zhang, L. Zhang, Z. Pu, R. Wang, H. Yu and D. Li, *Chem. Commun.*, 2020, **56**, 9056–9066.
- E. Stolovicki, R. Ziblat and D. A. Weitz, *Lab Chip*, 2018, **18**, 132–138.
- D.-C. Shin, Y. Morimoto, J. Sawayama, S. Miura and S. Takeuchi, *Sens. Actuators, B*, 2019, **301**, 127164.
- S. ten Klooster, J. van den Berg, C. Berton-Carabin, J. de Ruiter and K. Schroën, *Chem. Eng. Sci.*, 2022, **261**, 117993.
- N. Bhattacharjee, A. Urrios, S. Kang and A. Folch, *Lab Chip*, 2016, **16**, 1720–1742.
- Y. Fan, R. Boichot, T. Goldin and L. Luo, *AIChE J.*, 2008, **54**, 2796–2808.
- R. Ortiz, J. L. Chen, D. C. Stuckey and T. W. J. Steele, *ACS Appl. Mater. Interfaces*, 2017, **9**, 13801–13811.
- M. Chen, L. Wang, J. Chung, Y. Kim, P. Atluri and J. Burdick, *ACS Biomater. Sci. Eng.*, 2017, **3**, 3146–3160.